AIAA Journal
Vol. 48, No. 5, May 2010

Computational Modeling and Experiments of Natural Convection for a Titan Montgolfiere

Arnab Samanta,* Daniel Appelö,† and Tim Colonius‡
California Institute of Technology, Pasadena, California 91125
Julian Nott§
Nott Technology, LLC, Santa Barbara, California 93101
and
Jeffrey Hall¶
Jet Propulsion Laboratory, California Institute of Technology, Pasadena, California 91011

DOI: 10.2514/1.45854

Computational models are developed to predict the natural convection heat transfer and buoyancy for a Montgolfiere under conditions relevant to the Titan atmosphere. Idealized single- and double-walled balloon geometries are simulated using algorithms suitable for both laminar and (averaged) turbulent convection. Steady-state performance results are compared with existing heat transfer coefficient correlations. The laminar results, in particular, are used to test the validity of the correlations in the absence of uncertainties associated with turbulence modeling. Some discrepancies are observed, which appear to be primarily associated with temperature nonuniformity on the balloon surface. The predicted buoyancy for both the single- and double-walled balloons in the turbulent convection regime, predicted with standard two-equation turbulence models, showed trends similar to those with the empirical correlations. There was also good agreement with recently conducted experiments in a cryogenic facility designed to simulate the Titan atmosphere.

Nomenclature

c_p = specific heat
D = diameter of balloon
$\mathrm{D}/\mathrm{D}t$ = material derivative
$\mathbf{e}$ = unit vector in the direction of gravity
Gr = Grashof number
$\mathbf{g}$ = gravity vector
g = gravity
h = heat transfer coefficient
k = conductivity
Pr = Prandtl number
$\tilde{p}$ = departure from hydrostatic pressure
Ra = Rayleigh number
$\dot{Q}$ = total heat input
Q = nondimensional heat input; see Eq. (8)
$s(\mathbf{x})$ = distribution of heat
T = temperature
$\mathbf{u}$ = velocity vector
V_h = support $s(\mathbf{x})$, volume
β = coefficient of thermal expansion
ΔT = temperature differences with ambient temperature
ΔT_b = average temperature within the balloon
ΔT_s = average surface temperature
θ = normalized departure from ambient temperature
$\tilde{\theta}$ = nondimensional temperature change from the ambient; see Eq. (4)
ν = kinematic viscosity
ρ = density
ϕ = ratio of inner and outer diameters

Subscripts

i = inner
o = outer
∞ = ambient value

I. Introduction

SATURN'S moon Titan holds immense scientific interest, and a Montgolfiere, or hot air balloon, is an attractive aerobot configuration for its exploration. The cold dense atmosphere of Titan, with gravity of about one-seventh that of Earth, requires a significantly reduced heat input for a given balloon mass, compared with Earth. The smaller heat input also implies that natural convection, rather than radiation, will dominate the heat loss to the environment. For example, estimates using heat transfer correlations show that as little as 2 kW of power may be sufficient for certain scientific missions. However, more accurate predictions of turbulent convection are sought in order to carefully establish mission feasibility, uncertainty, and safety factors. The present paper reports on efforts to construct a detailed computational fluid dynamic/thermal model for this purpose.

Existing natural heat transfer correlations, described in detail in Sec. II, are very useful for system-level balloon models [1], but strictly apply only to simplified model problems such as the natural convection around a constant-temperature (or uniformly heated) sphere. Their application to hot air balloons, where the heat source and/or temperature fields are nonuniform, involves uncertainties that have not yet been assessed. Moreover, heat transfer correlations depend on whether the induced convective flow is laminar or turbulent. While the scale of the proposed Titan Montgolfiere (see Fig. 1) implies that natural convection will be turbulent, it is of interest to examine the correlations over a wide range of heat source strengths. The reason for this is that for the turbulent case, the

---

Presented as Paper 2806 at the AIAA Balloon Systems Conference, Seattle, WA, 4–9 May 2009; received 5 June 2009; revision received 29 January 2010; accepted for publication 2 February 2010. Copyright © 2010 by Arnab Samanta. Published by the American Institute of Aeronautics and Astronautics, Inc., with permission. Copies of this paper may be made for personal or internal use, on condition that the copier pay the $10.00 per-copy fee to the Copyright Clearance Center, Inc., 222 Rosewood Drive, Danvers, MA 01923; include the code 0001-1452/10 and $10.00 in correspondence with the CCC.

*Postdoctoral Scholar, Mechanical Engineering. Member AIAA.

†Postdoctoral Scholar, Applied and Computational Mathematics.

‡Professor, Division of Engineering and Applied Science. Senior Member AIAA.

§President. Senior Member AIAA.

¶Senior Engineer, Mobility and Robotic Systems. Senior Member AIAA.

computational models themselves involve turbulence models with adjustable parameters for which the uncertainty is not known a priori. For the laminar case, by contrast, any difference between the computational model and the heat transfer correlations can be attributed to the nonuniformity of temperature and heat flux at the balloon surfaces.

Thus, we consider laminar and turbulent natural convection around balloons with idealized heat sources, including single- and double-walled balloons with spherical geometries. The full governing equations describing conservation of mass, momentum, and energy are solved internally and externally to the balloon membrane(s). Estimates show that under relevant conditions, a Boussinesq approximation can be used, wherein the fluid is assumed to be nearly incompressible and the buoyancy force is proportional to temperature fluctuations. The flow is idealized as axisymmetric in order to reduce computational effort. To simplify the modeling we initially restrict our attention to steady-state performance at fixed altitude. For the turbulent cases, we use Reynolds-averaged Navier–Stokes (RANS) turbulence models. From the computed results, flow patterns are examined and steady-state temperature fields are analyzed to determine the buoyancy (lift force) as a function of heat input and to compare to existing (semi-empirical) heat transfer correlations. For the turbulent convection case, we validate the computational model by comparing the results with preliminary experiments performed in the Titan Sky Simulator$^{\mathrm{TM}}$ [2] facility designed to assess the buoyancy of Titan Montgolfiere prototypes under simulated cryogenic conditions comparable to the Titan atmosphere.

The remainder of the paper is organized as follows. In the next section, we review the relevant existing heat transfer correlations for natural convection internal and external to heated spheres and spherical annuli. In Secs. III and IV we present the computational and experimental methodology, respectively. In Sec. V we present the results of laminar simulations for spherical double-walled balloons and assess the accuracy of the individual heat transfer correlations internal and external to the balloon and in the gap. In Sec. VI, we present results for the turbulent convection case and compare our results to the aforementioned experimental results. Grid convergence studies and sensitivity of the computed results to model parameters is assessed and briefly summarized in Appendix A. The paper concludes with a brief summary of findings in Sec. VII.

II. Previous Theory and Correlations for Natural Convection Heat Transfer

A. Boussinesq Flow Model

In a typical balloon, the temperature difference between the balloon and ambient air, $T - T_\infty$, is small compared with the ambient temperature. Thus, it is appropriate to use the incompressible Boussinesq flow model:

$$\nabla \cdot \mathbf{u} = 0 \tag{1}$$

$$\rho_\infty \frac{\mathrm{D}\mathbf{u}}{\mathrm{D}t} + \nabla \tilde{p} = -\rho_\infty \frac{T - T_\infty}{T_\infty} \mathbf{g} + \mu_\infty \nabla^2 \mathbf{u} \tag{2}$$

$$\rho_\infty c_p \frac{\mathrm{D}T}{\mathrm{D}t} = k_\infty \nabla^2 T + \frac{\dot{Q}}{V_h} s(\mathbf{x}) \tag{3}$$

Note that we have neglected the temperature dependence of k and μ; this is valid to the same order as the Boussinesq approximation. Let

$$\tilde{\theta} = \frac{gD^3}{\nu_\infty^2} \theta = \frac{gD^3}{\nu_\infty^2} \frac{T - T_\infty}{T_\infty} \tag{4}$$

Then the equations may be rewritten in the nondimensional form

$$\nabla \cdot \mathbf{u} = 0 \tag{5}$$

$$\frac{\mathrm{D}\mathbf{u}}{\mathrm{D}t} + \nabla \tilde{p} = -\tilde{\theta}\mathbf{e} + \nabla^2 \mathbf{u} \tag{6}$$

$$\frac{\mathrm{D}\tilde{\theta}}{\mathrm{D}t} = \frac{1}{Pr} \nabla^2 \tilde{\theta} + \tilde{Q} \frac{D^3}{V_h} s(\mathbf{x}) \tag{7}$$

with the new parameter

$$\tilde{Q} = \frac{gD^2 \dot{Q}}{\rho c_p T_\infty \nu_\infty^3} \tag{8}$$

From these equations we may surmise that all the solutions to the problem may be determined by specifying just two nondimensional parameters: the Prandtl number and the nondimensional heat input $\tilde{Q}$. Note that the nondimensional temperature $\tilde{\theta}$ is in the form of a Grashof number:

$$Gr \equiv \frac{g\beta D^3 \Delta T}{\nu^2} \tag{9}$$

Substituting T_∞^{-1} for the coefficient of thermal expansion β and taking the temperature difference to be $T(\mathbf{x}) - T_\infty$, we recover $Gr = \tilde{\theta}$. However, we distinguish these parameters because the Grashof number typically corresponds to a *specific* temperature difference. We also have the relation $Ra = GrPr$, which relates $\tilde{\theta}$ to the Rayleigh number.

Under the Boussinesq approximation the net buoyancy, B may be expressed

$$B = \int (\rho_\infty - \rho) g \, \mathrm{d}V = \int \left(\frac{T - T_\infty}{T_\infty} \right) \rho_\infty g \, \mathrm{d}V$$

or, nondimensionally,

$$\frac{B}{\rho_\infty g V} = \frac{1}{V} \int \left(\frac{T - T_\infty}{T_\infty} \right) \mathrm{d}V \equiv \theta_b \tag{10}$$

where θ_b denotes the volume-averaged balloon temperature. The net buoyancy can be made nondimensional to yield the scaled temperature:

$$\frac{BD^3}{\rho_\infty \nu_\infty^2 V} = \tilde{\theta}_b$$

For a spherical balloon this reduces to

$$\tilde{\theta}_b = \frac{6B}{\pi \rho_\infty \nu_\infty^2} \tag{11}$$

B. Prediction of Net Buoyancy

Free convection around immersed bodies and within enclosures has been extensively studied. Based on laminar and turbulent boundary-layer theory, a local relation between the heat flux at the solid surface, the surface temperature, and the temperature outside the boundary layer is postulated:

$$\dot{q}'' = h(T_s - T_\infty) \tag{12}$$

where h is the convective heat transfer coefficient. Provided that variation of either the heat flux and or temperature over the surface is known, this relation may be integrated over the surface to obtain

$$\dot{Q} = A_s h_{\mathrm{avg}} (T_{s\mathrm{avg}} - T_\infty) \tag{13}$$

where the average is over the entire surface. Analytical solutions for simple bodies in laminar flow can be shown to lead to an equation for h_{avg} of the form

$$Nu = \mathrm{fun}(Ra, Pr, \text{geometry, surface conditions}) \tag{14}$$

where

$$Nu = \frac{h_{\mathrm{avg}} L}{k}, \qquad Ra = \frac{g(T_{s\mathrm{avg}} - T_\infty) L^3 \beta}{\nu \alpha} \tag{15}$$

L is a characteristic length of the body, and surface conditions refers to whether the temperature or heat flux is held constant along the surface or if it has some more complicated arrangement.

For turbulent flow and for laminar situations in which no analytical solution exists, relations of the form of Eq. (14) may still be expected to hold based on dimensional analysis. In those cases, data from many experiments may be used to determine an approximate analytical expression for the functional dependence. In what follows, the subscripts denote the two temperatures used to define the temperature difference in the Rayleigh number and definition of h_{avg}. The length scale for Rayleigh number is taken to be the outer balloon diameter D_o for external convection, the inner diameter D_i for internal convection, and the gap distance $(D_o - D_i)/2$ for gap convection.

C. External Convection

For the external convection, several correlations are available from the literature. Jones and Wu [1] recommend Campo's [3] correlation:

$$Nu_{D_o} = \begin{cases} 2 + 0.6Ra_{D_o}^{0.25} & Ra < 1.5 \times 10^8, \\ 0.1Ra_{D_o}^{0.340} & Ra \geq 1.5 \times 10^8 \end{cases} \tag{16}$$

which differs slightly from Churchill [4], who reports

$$\begin{cases} 2 + 0.461Ra_{D_o}^{0.25} & Ra < 1.5 \times 10^8, \\ 0.1Ra_{D_o}^{0.340} & Ra \geq 1.5 \times 10^8 \end{cases} \tag{17}$$

These correlations are developed for the situation of a external convection around a sphere of uniform temperature. In reality, the free convection inside the balloon determines the distribution of temperature and heat flux at the surface, which is nonuniform.

D. Internal Convection

For internal convection, Carlson and Horn [5] use

$$Nu_{D_i} = \begin{cases} 2.5(2 + 0.6Ra_{D_i}^{0.333}) & Ra < 1.35 \times 10^8 \\ 0.325Ra_{D_i}^{0.333} & Ra \geq 1.35 \times 10^8 \end{cases} \tag{18}$$

In the definitions of Nusselt number and Rayleigh number for the internal convection, we interpret the temperature difference as being specified between the bulk volume-averaged temperature within the balloon, T_b and the average surface temperature T_{Di}.

E. Convection Inside the Gap

For double-walled balloons, some researchers** use a correlation for gap convection of the form

$$Nu_\delta = 0.228Ra_\delta^{0.226} \tag{19}$$

where $\delta = (D_o - D_i)/2$ is the gap thickness. In this formula,†† the Nusselt number is based on the averaged heat flux over the average surface area of the two spheres, and the length scale is the gap width. A different formula is reported by Raithby and Hollands [6]:

$$Nu_\delta = 0.512\left(\frac{\phi^3(1-\phi)}{(1+\phi^{7/5})^5}\right)^{0.25} Ra_\delta^{0.25} \tag{20}$$

where $\phi = D_i/D_o$ for $Pr = 0.719$. Finally, Teertstra et al. [7] suggest corrections to the above to appropriately account for the low to mid Rayleigh number regimes. Their formula is

$$Nu^* = 2\sqrt{\pi}\frac{1}{1-\phi} + (Nu_{\text{tr}}^{-n} + Nu_{\text{bl}}^{-n})^{-\frac{1}{n}} \tag{21}$$

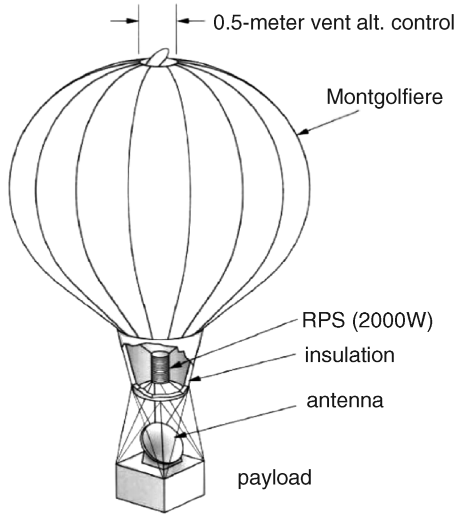

Fig. 1 Schematic of single-walled Jet Propulsion Laboratory Titan Montgolfiere.

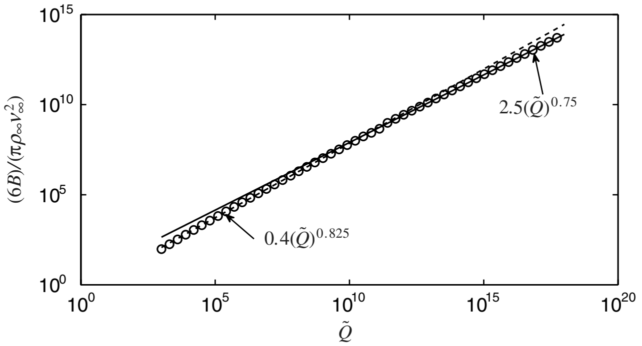

Fig. 2 Scaled net buoyancy versus scaled heat input.

where $n = 2$ is suggested and

$$Nu_{\text{tr}} = \frac{\sqrt{\frac{2}{\pi}}}{11520}\left(\frac{(1-\phi)^3}{\phi^2(1+\phi)}\right)Ra^*, \qquad Nu_{\text{bl}} = 0.521\frac{Ra^{*0.25}}{(1+\phi^{7/5})^{5/4}}$$

where Nu_{tr} and Nu_{bl} are the transition and boundary-layer Nusselt numbers, respectively. Here, the asterisk indicates that the length scale chosen for Nu and Ra is, in their case, the square root of the inner sphere area ($\sqrt{\pi}D_i$). Unlike the Raithby and Hollands [6] and Teertstra et al. [7] formulas, Jones and Wu's [1] formula does not explicitly depend on the ratio of diameters.

F. Combined Correlation

The above correlations may be combined to yield a prediction of the net buoyancy B. As before,

$$\frac{6B}{\pi\rho_\infty\nu^2} = \tilde{\theta}_b = \text{fun}(\tilde{Q}) \tag{22}$$

Note that if we base the Nusselt and Rayleigh numbers on D_o, we have the following relations:

$$Nu = \frac{\tilde{Q}Pr}{\pi\tilde{\theta}}, \qquad Ra = Pr\tilde{\theta}$$

The solution procedure is thus as follows. For a specified value of $\tilde{Q}$, we find the temperature change $\tilde{\theta}_{a-b}$ such that the appropriate convection relation between Nu_{a-b} and Ra_{a-b} is satisfied. Starting from the outside, we first find the ambient-to-outer-surface temperature change, the change across the gap, and the inner-surface-to-balloon-interior temperature change.

The result of this calculation is shown in Fig. 2 for a single-walled balloon, in which we plot the predicted scaled net buoyancy

---

[**] Private communication with J. Jones, 2009.

[††] This formula is equivalent to choosing an effective conductivity $k_{\text{eff}}/k = 0.228Ra_\delta^{0.226}$

$6B/\pi\rho_\infty\nu^2$ versus the scaled heat input $\tilde{Q}$. The transitions from laminar to turbulent correlations is evident at $\tilde{Q} \approx 10^{10}$. However, it is interesting to note that the change in overall exponent for $\tilde{Q}$ is very slight. Based on a best fit to the tabulated values, we can approximately propose

$$\frac{6B}{\pi\rho_\infty\nu^2} = \begin{cases} 0.4\tilde{Q}^{0.825} & \tilde{Q} < 10^{10}, \\ 2.5\tilde{Q}^{0.75} & \tilde{Q} > 10^{10} \end{cases} \tag{23}$$

III. Computational Methodology

For laminar convection computations, we directly solve (i.e. with no additional turbulence model) the governing Eqs. (5–7) representing conservation of mass, momentum, and energy using a conventional, staggered-mesh, incompressible finite volume scheme on a regular Cartesian mesh. The balloon geometry is modeled using an immersed boundary method [8,9], in which the boundary conditions at the surface of the balloon (no-slip) are satisfied by adding (regularized) body forces along the surface and determining their strength such that the no-slip boundary condition is enforced. The wall is presumed to be infinitely thin, such that the temperature distribution is continuous through the surface. The outer boundary of the computational domain is prescribed at ambient temperature and zero velocity, but it is placed sufficiently far away that it is verified to have no discernible impact on the flowfield or buoyancy.

In the laminar case, we considered spherical single- and double-walled balloons. The source region where heat is added is localized to a small spherical volume along the axis of symmetry and $0.6D_o$ below the center of the balloon. Some tests (not shown here) indicated that the results are not particularly sensitive to source locations below the center of the balloon, provided that the source region is small compared with the balloon diameter.

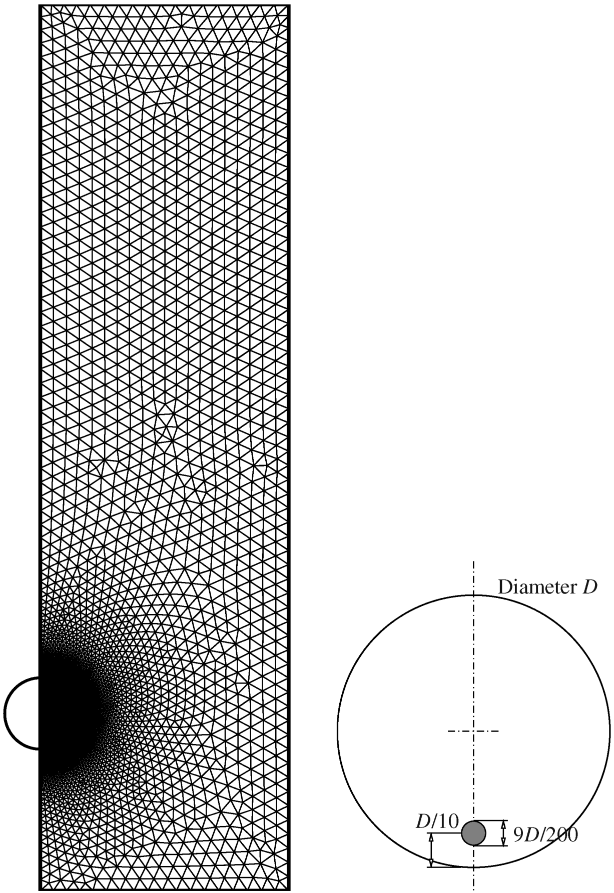

Fig. 3 Balloon geometry and base grid for the single-walled FLUENT simulations. Location and size of the heating element are also shown.

Table 1 Range of physical sizes D, heat inputs $\dot{Q}$, and the associated nondimensional heat input parameter as used in the turbulent simulations

	Cases					
	1	2	3	4	5	6
$\tilde{Q}/10^{17}$	0.0010	0.0060	0.0301	0.2008	1.0028	4.7752
$\dot{Q}$, W	250	250	150	1000	420	2000
D, m	0.4	1.0	2.9	2.9	10.0	10.0

The laminar computations were verified by comparing with analytical solutions for 1) transient pure conduction (gravity is switched off) for the given heat source and 2) superposed uniform flow over the sphere at a low Reynolds number. Moreover, for the balloon results presented here, several cases were run at progressively finer grid resolutions to check for grid convergence.

For turbulent calculations the commercial CFD code FLUENT was used together with different Reynolds-averaged Navier–Stokes turbulence models. The models solve for the (time-averaged) steady-state velocity and temperature fields. Different RANS models that have one or several tunable parameters are available. For the results presented in Sec. VI we have shown the two-equation turbulent models, viz., k-ε and k-ω [10], in which the solution of two separate transport equations allows the turbulent velocity and length scales to be independently determined. The two-equation models seem to better predict the turbulent correlations, discussed in Sec. II. The constants in the models were also kept at their default (factory) settings. However, to assess the sensitivity to the turbulence model, for some particular setups we have used the other turbulence models and perturbed the parameter settings in the standard k-ε model (this is described in Appendix A). For the double-walled turbulent simulations we have only used the k-ω model, which seems to give the best results (with respect to the correlations) for the single-walled balloon.

Similar to the laminar case, the turbulent calculations were also performed for spherical single- and double-walled balloons and are depicted in Fig. 3, in which the location of the heat source is also shown. For a given set of flow parameters, the nondimensional heat source parameter (8) can be varied by either changing the heat input $\dot{Q}$ or the balloon diameter D. In our single-walled simulations of Sec. VI.A we have varied both, corresponding to nondimensional heat inputs $\tilde{Q}$ in the range of 9.6×10^{13} to 4.8×10^{17}. The ranges of values used are listed in Table 1. The limiting values of $\dot{Q}$ and D [2000 W and 10 m, respectively (gives $\tilde{Q} = 4.8 \times 10^{17}$)] correspond to a full-scale Titan Montgolfiere. The various ways of obtaining the same $\tilde{Q}$ provides a useful numerical check for these simulations. Note that values in the range of 10^{14} to 10^{15} correspond to the scaled experiments, as discussed in the next section. For the double-walled cases of Sec. VI.B, a second wall is used, which is defined using a gap thickness parameter $\phi = D_i/D_o$, where D_o and D_i are, respectively, the outer and inner diameters of the double-walled balloon. Here, we restrict ourselves to a particular heat input value, $\tilde{Q} = 5.97 \times 10^{14}$, while concentrating on how changing ϕ affects the buoyancy.

The grid convergence studies for both the laminar and turbulent simulations appear in Appendix A.

IV. Experimental Methodology

Figure 3 shows the balloon geometry and base grid for the single-walled FLUENT simulations. Location and size of the heating element are also shown. Practical data was acquired using the Titan Sky Simulator [2]. The simulator is a box 2.5 m square and 5 m tall (see Fig. 4). It is highly insulated (see Fig. 4) and the interior is cooled by adding liquid nitrogen, which evaporates filling the interior with nitrogen gas somewhat above its boiling point.

The balloon was flown at various temperatures down to −170 C/103 K. The resulting thermophysical properties of N_2 are given in Table 2. While this differs slightly from the target ambient temperature of Titan (which is about 20 deg colder), it is significant

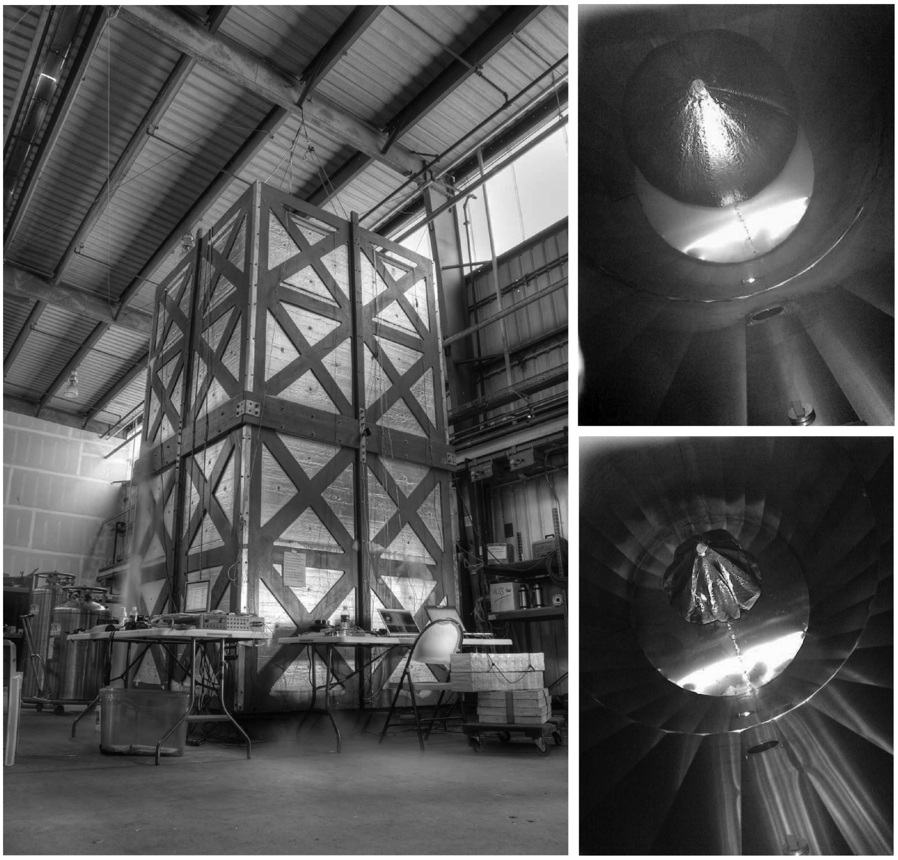

Fig. 4 Exterior view of the Titan Sky Simulator [2] (left) and view of the balloon inside the simulator before start of experiment (bottom right) and flying at low temperature (top right).

that the balloon was flown in conditions in which only a negligible amount of the total heat transfer was by radiation. For balloons flying in terrestrial conditions, the majority of heat transfer is by thermal radiation. However, radiation varies with the fourth power of absolute temperature. At Titan's low absolute temperature, radiation falls dramatically and is of little importance. This balloon was flown at temperatures low enough that radiation was small.

The balloon was heated using a resistance heater. This was inside the balloon but did not touch it at any point. Care was taken to ensure that the heater had a large enough surface area so that almost all heat entered the balloon by convection. The surface temperature of the heater was monitored to confirm that it was cold enough that only a negligible amount of heat was being transferred by thermal radiation. The balloon was suspended by a line from above, which passed through the crown. However, it was not attached to the crown, but supported the balloon only at the base. In this way, the balloon flew as it normally would, with the load carried only by the mouth. Fans and interior baffling were used to mix the interior gas to achieve a uniform temperature, while at the same time minimizing wind in the region where the balloon was flying.

Twenty-four thermocouples where installed on the balloon and throughout the simulator. These measured the internal temperature of the balloon, the temperature of the balloon film at several points, and the ambient temperature of the walls and bulk gas. The measurements that are of greatest interests are the temperature differences between the balloon and its surroundings. So the thermocouples were installed in a differential mode, with hot junctions attached to the points of interest and the cold junctions all clamped together to a common temperature reference point, although electrically isolated. This has the advantage that most of the thermocouple wire is copper, reducing the resistance in the long run to the external measuring equipment.

Table 2 Physical properties for nitrogen at 103 K used in the turbulent simulations

Property	Value	Unit
p_∞	101,325	Pa
ρ_∞	3.368	kg/m^3
T_∞	103.15	K
C_p	1068.7	J/kg/K
ν	$2.229 \cdot 10^{-6}$	m^2/s
k	0.0112	W/m/K
Pr	0.719	——
g	9.82	m/s^2

V. Laminar Convection on Single- and Double-Walled Balloons

Results from laminar simulations employing a range of (non-dimensional) heat inputs and gap widths are shown in Figs. 5–7, in

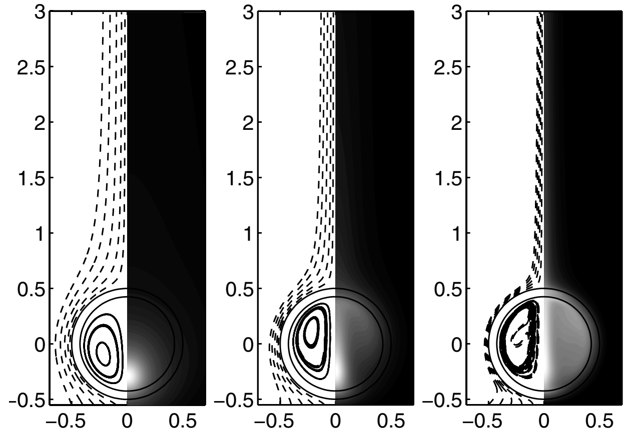

Fig. 5 Steady-state streamlines (left) and temperature contours (right) for a double-walled balloon with $\phi = 0.85$, and heat inputs, from left to right, of $\tilde{Q} = 10^4$, 10^6, and $15 \cdot 10^7$. The grayscale map is linear and ranges from $\tilde{\theta} = 0$ to $6.4 \cdot 10^3$, $2.8 \cdot 10^5$, and $1.2 \cdot 10^7$ (left to right).

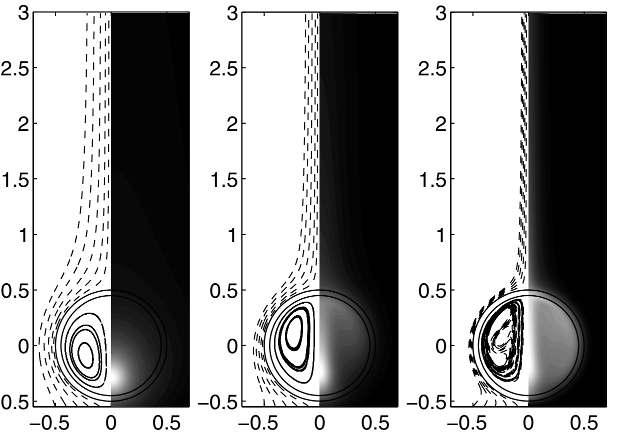

Fig. 6 Same as Fig. 5, but with $\phi = 0.90$. The grayscale map is linear and ranges from $\tilde{\theta} = 0$ to $6.3 \cdot 10^3$, $2.5 \cdot 10^5$, and $1.1 \cdot 10^7$ (left to right).

which streamlines and temperature contours are drawn at steady state in order to discuss qualitative features of the convective flow.

For the lowest heat inputs, the flow patterns are substantially different; not much flow is generated and temperature contours are reminiscent of the pure conduction problem. However, as the heat input is increased, a stronger and progressively thinner plume is generated inside the balloon. The temperature around the periphery of the balloon becomes progressively more nonuniform, with a strong hot spot at the top of the balloon. The external boundary layer also becomes progressively thinner. Once the plume assumes the more slender shape, its shape remains the same, even when the heat input is increased significantly (see Fig. 7). The shape of the plume does not depend significantly on the gap size, but for the largest gap considered, it appears as if the temperature is more evenly distributed, especially for stronger heat inputs.

In Fig. 8 the results from the laminar simulations are presented in terms of Rayleigh and Nusselt numbers at steady state, corresponding to the temperature difference between the internal volume-averaged temperature and the inside-sphere surface averaged value. These data are compared with the internal heat transfer correlation given by Eq. (18). At very low Rayleigh numbers the simulations collapse onto a constant Nusselt number, corresponding to the conduction limit. Over the range of Rayleigh numbers for a thin laminar convection boundary layer, there is progressively better agreement with the *turbulent* correlation. It is unclear why the laminar correlation performs so poorly or why the results agree better with the turbulent one. We can also observe that the results do not collapse to a single correlation independent of the gap thickness. This indicates that the internal temperature *distribution* is changed as the gap thickness is changed, and this provides some guidance as to the sensitivity of the correlations to the details of the temperature distribution (for the laminar case).

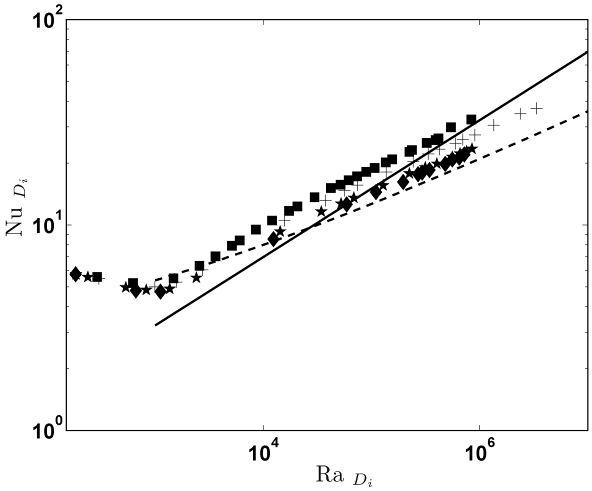

Fig. 8 Comparison between steady-state laminar simulation results and the internal convection correlation (18) (■, $\phi = 1$; +, $\phi = 0.95$; ◆, $\phi = 0.90$; and *, $\phi = 0.85$). The dashed line represents the laminar (low Rayleigh number) correlation and the solid line represents the turbulent (high Rayleigh number) one.

In Fig. 9 convection in the gap is considered. The correlation suggested by Teertstra et al. [7] is compared with the simulation results. The simulations result in relatively low gap Rayleigh numbers and appear to be closer to the conduction limit than the laminar boundary-layer regime implied by Eq. (19). In the pure conduction limit ($Ra \to 0$), the simulation results agree with Eq. (21), but fail to be captured by the correlation as convection begins to occur. A possible explanation of the discrepancy could again be the nonuniform temperature distribution.

In Fig. 10 the external correlation (17) is compared with simulation results for double- and single-walled balloon cases. Despite the fact that the correlation is derived for uniformly heated sphere, the simulation data (with nonuniform temperature) agree relatively well with the correlation, especially at the higher values of Rayleigh number considered.

In Fig. 11 all results from the laminar simulations are collected and expressed in terms of the nondimensionalized heat input and buoyancy. The solid black line is the correlation (23) for the single-walled balloon. As can be seen, the simulation data for the single-walled balloon line up quite well with the overall correlation. The significantly increased buoyancy (and thus payload) in double-walled designs is also apparent. This represents an increase of almost 80% in some cases, although, owing to the relatively poor performance for the gap convection (see Fig. 9) prevents the theory from giving reliable double-walled predictions.

Given the double-walled simulation results, we may offer a least-squares fit to a power-law model of the form

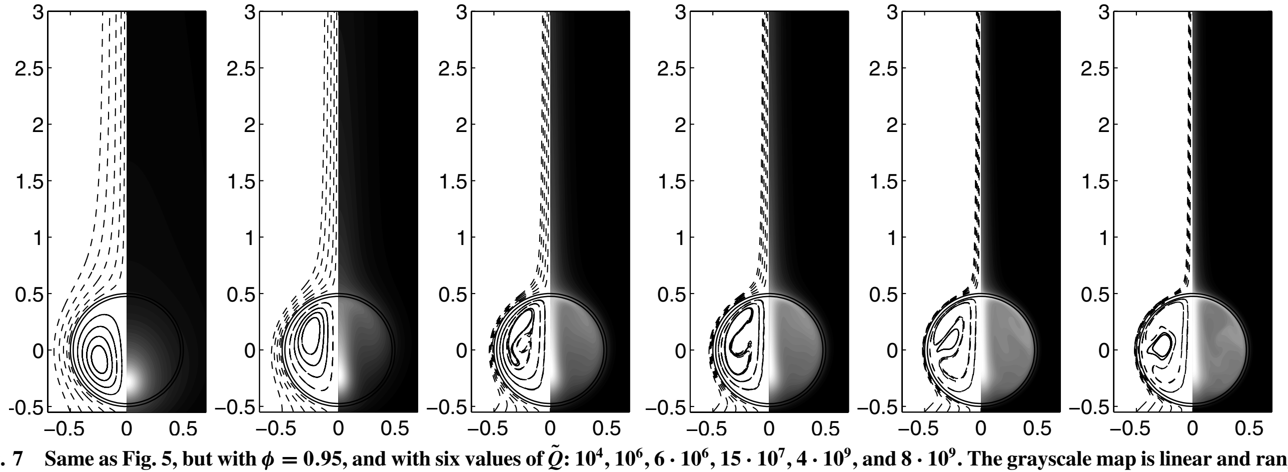

Fig. 7 Same as Fig. 5, but with $\phi = 0.95$, and with six values of $\tilde{Q}$: 10^4, 10^6, $6 \cdot 10^6$, $15 \cdot 10^7$, $4 \cdot 10^9$, and $8 \cdot 10^9$. The grayscale map is linear and ranges from $\tilde{\theta} = 0$ to $6.2 \cdot 10^3$, $2.3 \cdot 10^5$, $4.7 \cdot 10^6$, $9.2 \cdot 10^6$, $9.2 \cdot 10^7$, and $1.7 \cdot 10^8$ (left to right).

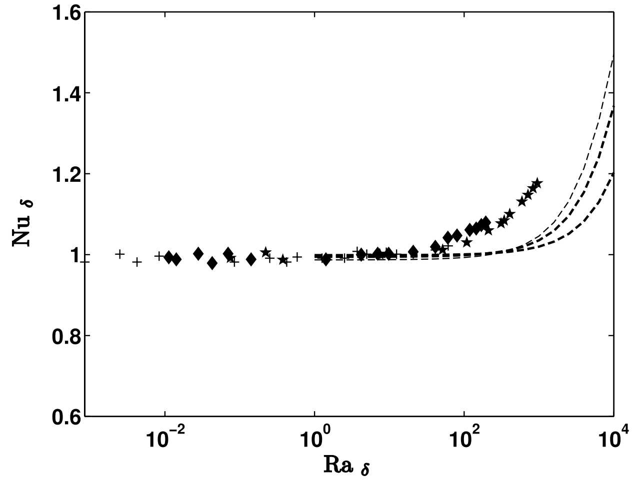

Fig. 9 Comparison between steady-state laminar simulation results and correlations for gap convection (■, $\phi = 1$; +, $\phi = 0.95$; ◆, $\phi = 0.90$; and *, $\phi = 0.85$). The dashed, dashed-dotted, and dotted lines are curves describing correlation (21) with $\phi = 0.95$, 0.90, and 0.85.

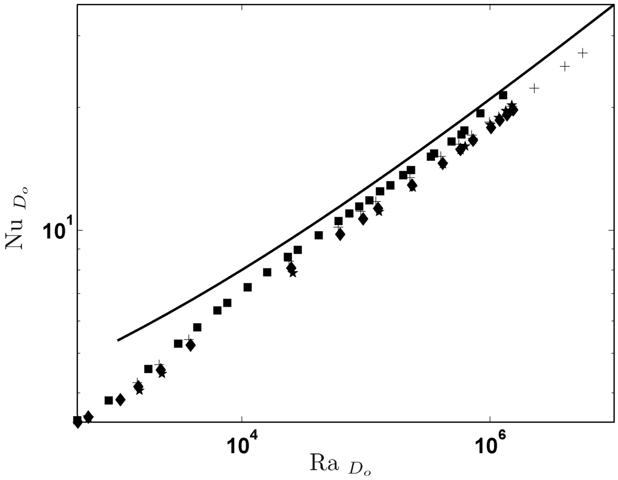

Fig. 10 Comparison between steady-state laminar simulation results and external correlations (■, $\phi = 1$; +, $\phi = 0.95$; ◆, $\phi = 0.90$; *, and $\phi = 0.85$). The solid line is the correlation (17).

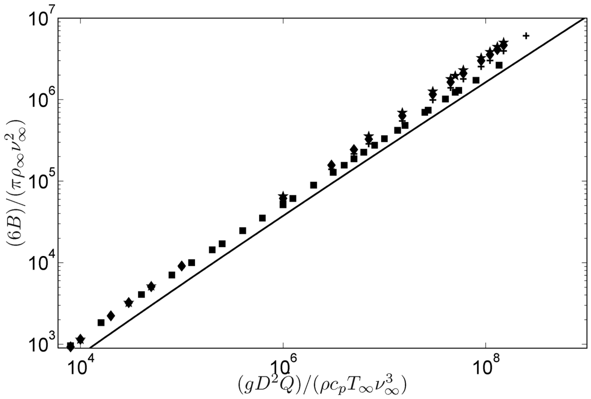

Fig. 11 Comparison between laminar simulation results and correlations. Displayed is the nondimensional buoyancy against nondimensionalized heat input. The ■, +, ◆ and * represent computational results for balloons with $\phi = 1$, 0.95, 0.90, and 0.85. The solid line is the predicted buoyancy using Eq. (23).

Table 3 Values of the parameters in model (24) for laminar convection in double-walled balloons

	Single wall	Double wall	Double wall	Double wall
δ	1.0	0.95	0.90	0.85
χ_2	0.752	0.840	0.858	0.867
χ_1	0.806	0.530	0.444	0.412

$$\theta_b = f(\tilde{Q}) = \chi_1 \tilde{Q}^{\chi_2} \tag{24}$$

The values are given in Table 3.

VI. Turbulent Convection: Comparison of Experiment, Computation, and Theory

A. Single-Walled Results

In this section, we compare results from turbulent simulations using the FLUENT model for single-walled balloons with the experiments performed in the Titan Sky Simulator and the empirical correlation (23). In Table 4 heat input and measured lift values (in SI units) from experiments are reported. Using the thermophysical properties of nitrogen (Table 2), we may convert the heat input and lift to nondimensional values, $\tilde{\theta}$ and $\tilde{Q}$, respectively, and plot them against the combined correlation in Fig. 12. It should be noted that the different ambient temperatures lead to different values of nondimensional heat input, even when the physical heat input is held constant. Also plotted in the figure are the FLUENT simulation results computed using the standard k-ε and k-ω RANS turbulence models. In Table 5 the relative deviations (in %) from the correlation are also reported.

The experimental and computational results line up well with the empirical correlation. This provides, for the first time, a direct confirmation of the turbulent internal and external heat transfer correlations leading to Eq. (23) and validates their use for system-level models for the Titan Montgolfiere. The correlations underpredict the simulation data (less buoyancy) from a low of 28% to as much as 59% (see Table 5), depending on the nondimensional heat input. This shows that the correlations are conservative and that a balloon designed using them could be equipped with larger payload than predicted.

To further understand the reason behind such deviation, we have separately plotted the simulation data points against the external and internal correlations in Figs. 13 and 14, respectively. As noted in Sec. II, both the correlations assume a uniform wall temperature distribution. However, in the turbulent regime, for the range of heat inputs considered, that is very much not the case, especially for the balloon interior wall. This is reflected in Fig. 14, in which the data points lie significantly off from the correlation. The temperature distribution is more uniform for the exterior wall, which yields better agreement in Fig. 13 for the external correlation. Apart from the nonuniform temperature distribution, uncertainty in the FLUENT turbulence models could also result in significant discrepancy. As for the experimental results, there is some scatter, especially for two outliers, and it would be useful to follow up these preliminary experiments to obtain a better understanding of repeatability and uncertainty in the data.

Table 4 Experimental data from the Titan Sky Simulator; values in parentheses are relative deviations (in %) from the correlation

Q, W	T_∞, K	gB, kg
198	103	0.304 (31)
422	158	0.327 (10)
422	136	0.453 (37)
422	144	0.561 (77)
195	120	0.274 (34)
195	148	0.184 (5)
195	156	0.168 (0)
195	189	0.095 (−35)

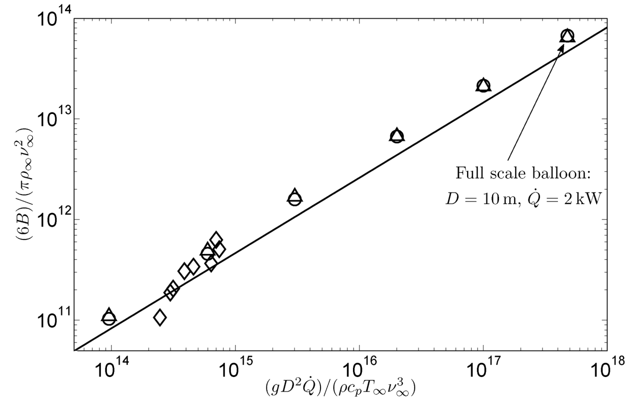

Fig. 12 FLUENT turbulent simulation results, experiments and correlation. Displayed is the nondimensional buoyancy against nondimensionalized heat input for: △, *k*-*ε* model; ○, *k*-*ω* model; ◇, experimental data; and solid line, combined correlation (23). The values at the right boundary of the plot correspond to a full-sized balloon.

The numerical values of the computational predictions are reported in Table 5. The highest value for $\tilde{Q}$ used in the computations is equivalent to that of a 10 m balloon flying in nitrogen at 103 K with a 2000 W heat source. To get a quantitative feel, if the computational result of the rightmost data point is converted to dimensional lift, we find that such a balloon is predicted to yield a lift of 58 kg under the conditions of Table 2.

B. Double-Walled Results

In this section, we describe the simulations for double-walled balloons. The second wall provides an additional insulating layer by trapping gas inside the gap, which increases the overall lift for the same heat input. Such a configuration is thus beneficial for the deployment of a Montgolfiere. However, there appears to be an optimum gap thickness, as explained below.

The nondimensional heat input chosen lies near the experimental data points of the Titan Sky Simulator, as described in Sec. IV. Only the *k*-*ω* RANS turbulence model is used. Results for different ϕ are reported in Table 6. It also shows the deviation from the combined correlation when each of the three gap correlations, as described in Sec. II.E, are used. Figure 15 overlays the double-walled FLUENT data on the $\tilde{Q}$–$\tilde{\theta}$ plane, where the combined correlation using the gap correlation of Jones and Wu [1] [see Eq. (19)] is also shown for various gap thicknesses. Figure 16 plots the same against ϕ.

The insulation feature of the second wall is evident from the buoyancy gain over the single-walled design. For the range of gap thicknesses studied, this is more than a 70% gain (see also Fig. 15). The gap, because of the trapped gas inside, provides insulation that reaches an optimum as the gap thickness is slowly increased (or ϕ decreased). Beyond this optimum value, the walls are too far apart to maintain a steady convection layer, and thus the insulation effect reduces. Instead, the inner and outer walls develop separate boundary layers. Beyond a certain gap thickness, the effect of the gap is expected to disappear and the net buoyancy is expected to stabilize to some value. This is roughly observed in the FLUENT simulation data in which a peak buoyancy is achieved at around $\phi = 0.925$, while little change is seen for lower ϕ values. This is also visualized in Fig. 16.

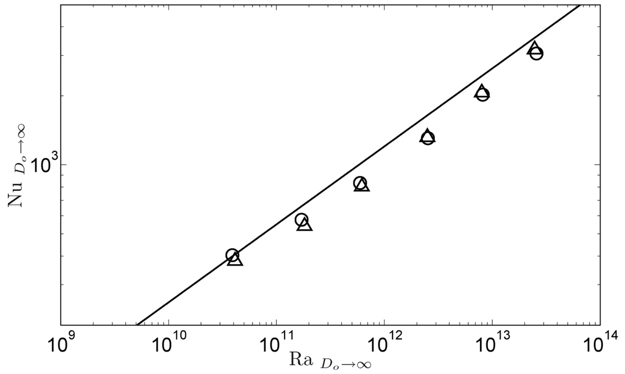

Fig. 13 Comparison between FLUENT turbulent simulation results and external correlation (17). △, *k*-*ε* model; ○, *k*-*ω* model; and solid line, external correlation (17).

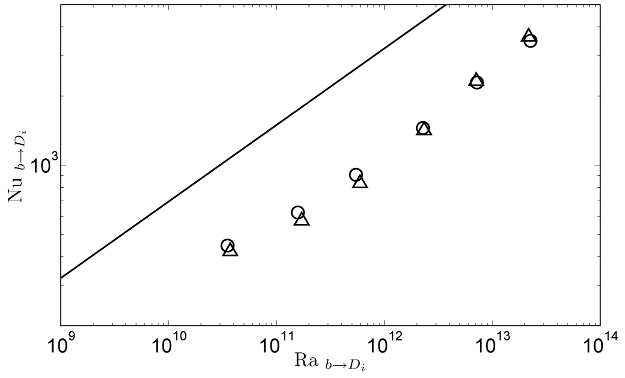

Fig. 14 Same as Fig. 13, but for internal correlation (18).

The double-walled correlations are closer to the simulation data than the single-walled data, but quite interestingly, they mostly overpredict the buoyancy (Table 6). When compared with the single-walled correlations, a second wall introduces additional approximations due to nonuniform temperature distributions at both of the walls. Among the different correlations, Jones and Wu's [1] [Eq. (19)] gap correlation, with the simplest algebraic structure, does the best, especially for higher values of ϕ. The correlation by Teertstra et al. [7] [Eq. (21)], although it consistently overpredicts the

Table 6 Computed nondimensional buoyancy for the double-walled FLUENT simulations for $\tilde{Q} = 5.97 \times 10^{14}$ using the *k*-*ω* model

	Cases[a]				
	1	2	3	4	5
ϕ	0.95	0.925	0.9	0.875	0.85
$6B/\pi\rho_\infty\nu_\infty^2)/10^{13}$	0.0783 (71.3)	0.0833 (82.3)	0.0821 (79.6)	0.0811 (77.6)	0.0790 (73.0)
Teertstra et al. [7]	−20.0	−17.2	−19.1	−20.1	−22.0
Raithby and Hollands [6]	−19.1	−14.2	−15.8	−17.1	−19.7
Jones and Wu [1]	0.3	−0.3	−6.8	−11.7	−17.0

[a] Values in parentheses are relative gain (in %) from the single-walled design; also shown are the relative deviations (in %) from the combined correlation when using the various gap correlations.

Table 5 Computed nondimensional buoyancy $(6B/\pi\rho_\infty\nu_\infty^2)/10^{13}$ from FLUENT simulations for the two-equation models; values in parentheses are relative deviation (in %) from the correlation

	Cases					
	1	2	3	4	5	6
$\tilde{Q}/10^{17}$	0.0010	0.0060	0.0301	0.2008	1.0028	4.7752
k-*ε*	0.0110 (36.4)	0.0491 (55.4)	0.1686 (59.1)	0.6724 (53.7)	2.1016 (44.3)	6.4618 (38.2)
k-*ω*	0.0103 (28.4)	0.0457 (44.6)	0.1587 (49.8)	0.6688 (52.9)	2.1382 (46.9)	6.7204 (43.8)

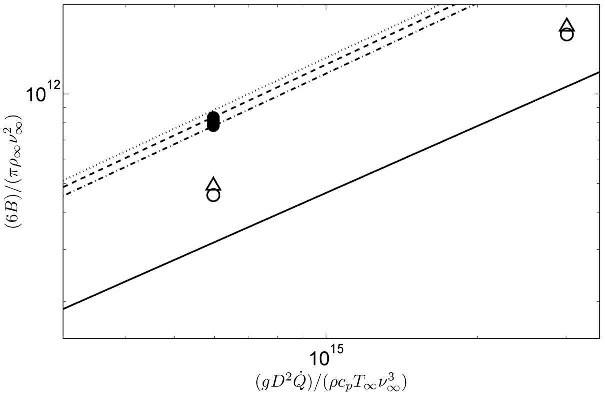

Fig. 15 FLUENT turbulent simulation results and correlation. Simulation data for: △, k-ε single-walled model; ○, k-ω single-walled model and ●, k-ω double-walled model for various ϕ. Also shown are the correlations: solid line, combined single wall [Eq. (23)]; dotted-dashed line, combined double wall for $\phi = 0.95$; dashed line, combined double wall for $\phi = 0.925$; and dotted line, combined double wall for $\phi = 0.9$. The gap correlation used is due to Jones and Wu [1] [Eq. (19)].

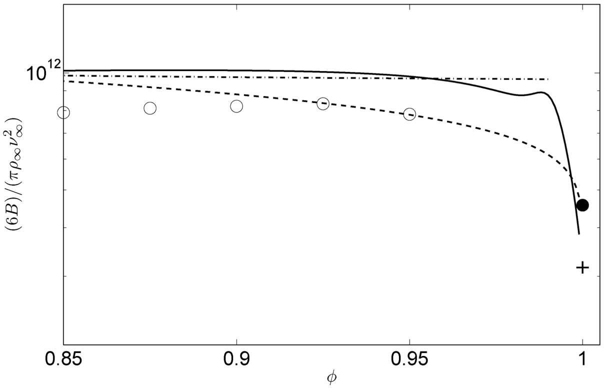

Fig. 16 FLUENT double-walled turbulent simulation results and correlation for $\tilde{Q} = 5.97 \times 10^{14}$. ○, k-ω double-walled model and ●, k-ω single-walled model ($\phi = 1.0$). Also shown is the combined correlation for different gap correlations: solid line, Teertstra et al. [7] [Eq. (21)]; dashed-dotted line, Raithby and Hollands [6] [Eq. (20)]; dashed line, Jones and Wu [1] [Eq. (19)]; and +, combined single-walled correlation.

simulations, actually captures the shape of the simulation data best, as can also be noted from Table 6. Here, it is worth remembering that Teertstra et al.'s [7] correlation is optimized to give better answers near the low- and mid-Ra regimes and so it is not probably surprising to see it doing poorly here. Raithby and Hollands [6] [Eq. (20)] lie somewhere in between.

VII. Conclusions

Computational models to predict the natural convection and buoyancy of idealized hot air balloons have been developed and compared with theoretical/empirical heat transfer correlations and experimental data from the Titan Sky Simulator cryogenic facility. Separate algorithms were used for the laminar and turbulent regimes, and the latter used standard Reynolds-averaged turbulence models.

Since the laminar simulations involve no modeling uncertainties beyond the idealization of the heat source, they may be used to establish the detailed credentials of the heat transfer correlations. While overall predictions for the single-walled balloons were satisfactory, gap convection correlations did not provide satisfactory agreement with the simulations.

The turbulent results showed similar trend when compared with the empirical correlation for a broad range of heat inputs, corresponding from model to full-scale balloons being designed for exploration of Titan. The higher predicted buoyancy of the simulations was attributed to the simplifying assumptions made in the correlations. These correlations were developed for spherical objects with uniform wall temperature. In our simulations the wall temperature remained highly nonuniform for the balloon inner wall and less so for the outer wall. For the single-walled combined correlation, the major error then came from the internal correlation relation. For the double-walled results, the presence of an additional wall changed these errors in a way in which the correlations slightly overestimated the simulations. In addition, there were uncertainties associated with the various turbulence models.

Our future work will extend the turbulent models to other balloon shapes, mixed forced/natural convection around ascending and descending balloons, and to examine heat losses and changes in buoyancy associated with vents and other geometrical variations of the balloon.

Appendix A: Sensitivity Analysis

Figure A1 shows relative errors (made relative by the average temperature at steady state) in the average temperature on the outer surface for a balloon with $\phi = 0.9$ and $\tilde{Q} = 10^5$ for two laminar computations using 52×200 and 104×400 grid points. The errors were computed using a reference solution with 208×800 grid points. The coarser grid yields a relative error of about 1% and, as expected, the finer grid yields a four-times-smaller error: namely, 0.25%. The figure also shows the (much smaller) relative errors in the average temperature as the location of the outer boundary is varied.

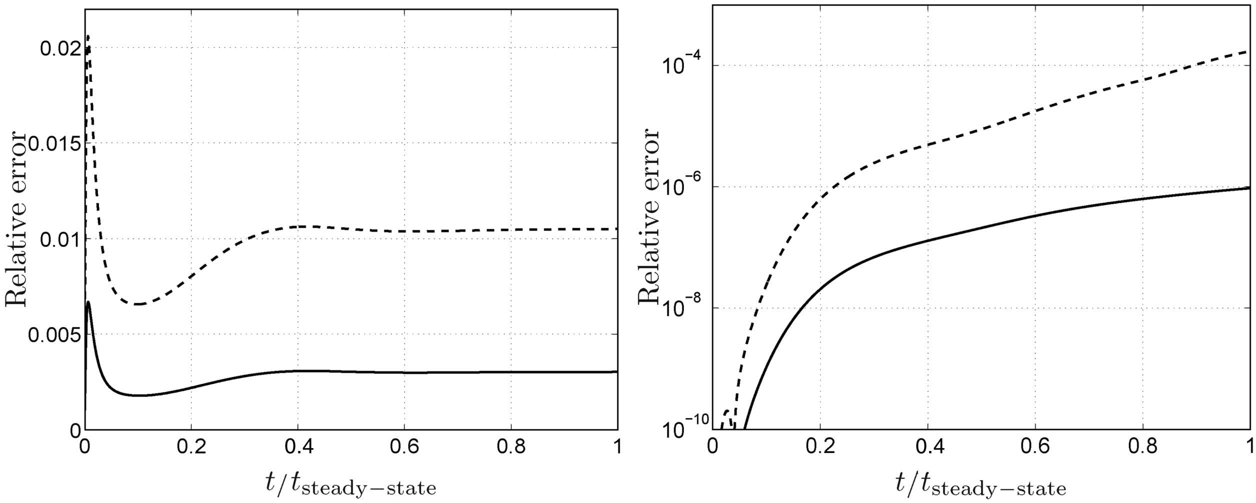

Fig. A1 Relative errors in the average temperature on the outer surface for a balloon with $\phi = 0.9$ and $\tilde{Q} = 10^5$ for two computations using 52×200 (dashed) and 104×400 (solid) grid points (left) and as the location of the outer boundary is varied (right).

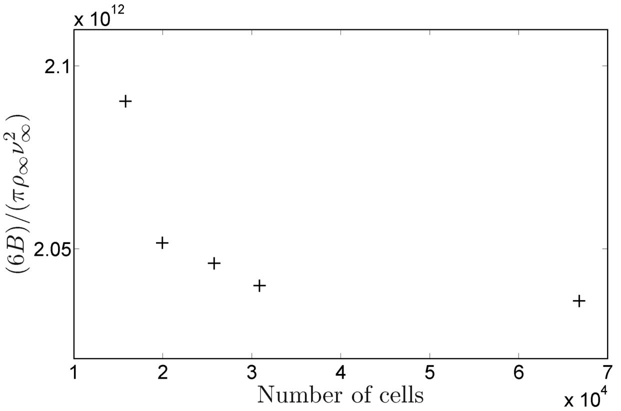

Fig. A2 Test for FLUENT grid convergence. Nondimensional buoyancy plotted against the number of cells used in the FLUENT mesh.

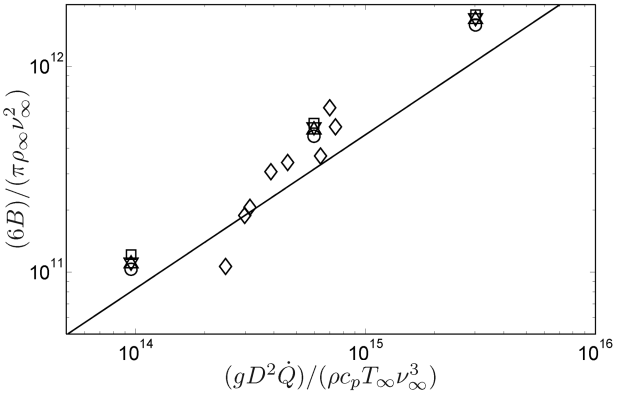

Fig. A3 Nondimensional buoyancy against nondimensionalized heat input for the following turbulence models: △, *k*-*ε*; ○, *k*-*ω*; ▽, Reynolds stress; □, Spalart; Allmaras◇, experimental data; and solid line, combined correlation.

As many different $\tilde{Q}$ are used for the computations above and it would be inconvenient to assess the independence of the discretization for all of them, the following approach was taken. A set of $\tilde{Q}$ (starting with the largest) was chosen, and for each of those, a sufficiently fine grid and sufficiently-far-away placement of the outer boundary was found (requiring the relative error to be less than 1%). That discretization and boundary placement were then used for the smaller appropriate $\tilde{Q}$.

Figure A2 shows the grid convergence study for the single-walled turbulent simulations using FLUENT. In this test case, we have used a balloon of $D = 1.4$ m with a heat input of $\dot{Q} = 2$ kW and the k-ω turbulence model. As can be seen in the figure, with increasing mesh resolution, which is achieved by increasing the number of triangular cells in the mesh, we obtain near mesh independence. For double-walled simulations, the balloon gap is remeshed as finely as required to effectively capture the boundary layers therein. These simulations become quite expensive for, say, $\phi > 0.95$.

To assess the sensitivity of the computed turbulent correlations we used different RANS models (Spalart–Allmaras, k-ε, k-ω, and Reynolds stress) with their respective factory setups to predict the buoyancy. The results in terms of computed nondimensional buoyancy from this study are reported in Fig. A3. As commented earlier, the two-equation models are generally seen to give the best prediction, while the single-equation Spalart–Allmaras model overpredicts the buoyancy by 15%, on an average, as compared with the two-equation models. The predictions from the Reynolds-stress model lie in between. In Fig. A3 the nondimensional buoyancy computed from data from the Titan Sky Simulator is also plotted. As reported above, the experimental data also fall in the vicinity of the correlation, but with more spread than the computational models. Finally, for the k-ε model, we perturbed the adjustable parameters C_μ, C_1-ε, and C_2-ε up or down 10% relative to their factory-settings values. We also used the two other available k-ε models, RNG and Realizable, to predict the buoyancy. The results, which can be found in Table A1, show that the output is relatively insensitive to such perturbations.

Acknowledgments

This work was supported by NASA Jet Propulsion Laboratory (JPL) under JPL award no. 1294409 and JPL award no. 1363442.

References

[1] Jones, J., and Wu., J.-J., "Performance Model for Reversible Fluid Balloons," AIAA Paper 95-1608-CP, 1995.

[2] Nott, J., and Rand, J., "The Titan Sky Simulator$^{\text{TM}}$ Test Facility," AIAA Balloon Systems Conference, AIAA Paper 2007-2625, Williamsburg, VA, May 2007.

[3] Campo, A., "Correlation Equation for Laminar and Turbulent Natural-Convection from Spheres," *Wärme- und Stoffübertragung*, Vol. 13, Nos. 1–2, 1980, pp. 93–96. doi:10.1007/BF00997638

[4] Churchill, S., "Free Convection Around Immersed Bodies," *Heat Exchanger Design Handbook*, Hemisphere, New York, 1983.

[5] Carlson, L. A., and Horn, W. J., "New Thermal and Trajectory Model for High-Altitude Balloons," *Journal of Aircraft*, Vol. 20, No. 6, 1983, pp. 500–507. doi:10.2514/3.44900

[6] Raithby, G. D., and Hollands, K. G. T., "A General Method of Obtaining Approximate Solutions to Laminar and Turbulent Free Convection Problems," *Advances in Heat Transfer*, Vol. 11, Academic Press, New York, 1975, pp. 265–315.

[7] Teertstra, P. M., Yovanovich, M. M., and Culham, J. R., "Analytical Modeling of Natural Convection in Concentric Spherical Enclosures," *Journal of Thermophysics and Heat Transfer*, Vol. 20, No. 2, 2006, pp. 297–304. doi:10.2514/1.16811

[8] Taira, K., and Colonius, T., "The Immersed Boundary Method: A Projection Approach," *Journal of Computational Physics*, Vol. 225, No. 2, Aug. 2007, pp. 2118–2137. doi:10.1016/j.jcp.2007.03.005

[9] Colonius, T., and Taira, K., "A Fast Immersed Boundary Method Using a Nullspace Approach and Multi-Domain Far-Field Boundary Conditions," *Computer Methods in Applied Mechanics and Engineering*, Vol. 197, April 2008, pp. 2131–2146. doi:10.1016/j.cma.2007.08.014

[10] Launder, B. E., and Spalding, D. B., *Lectures in Mathematical Models of Turbulence*, Academic Press, London, 1972.

R. Rangel
Associate Editor

Table A1 Perturbation of *k*-*ε* at $\tilde{Q} = 9.55 \times 10^{13}$[a]

k-ε model	C_μ	C_1-ε	C_2-ε	TKE Pr	TDR Pr	Energy/wall Pr	$(6B/\pi\rho_\infty\nu_\infty^2)/10^{11}$	% diff
STD	0.09	1.44	1.92	1	1.3	0.85	1.095	36.4
STD	0.081	1.44	1.92	1	1.3	0.85	1.099	36.9
STD	0.09	1.58	1.92	1	1.3	0.85	1.090	35.8
STD	0.09	1.44	2.11	1	1.3	0.85	1.094	36.3
STD (visc. heat)	0.09	1.44	1.92	1	1.3	0.85	1.099	36.9
RNG	0.084	1.42	1.68	——	——	0.85	1.073	33.7
Realizable	——	——	1.9	1	1.2	0.85	1.074	33.8

[a] STD is standard, RNG is renormalization group, TKE is turbulent kinetic energy, and TDR is turbulent dissipation rate.